
This manuscript is a EarthArxiv preprint and had been submitted for publication in the **Basin Research**. Please note that this manuscript has **not been peer-reviewed**. Subsequent versions of this manuscript may, thus, have slightly different content. If accepted, the final version of this manuscript will be available via the “Peer-reviewed Publication DOI” link on the right-hand side of this webpage. Please feel free to contact any of the authors directly; We welcome your feedback.

1 Syn-Depositional Halokinesis in the Zechstein Supergroup
2 (Lopingian) Controls Triassic Minibasin Genesis and Location

3 Amir Joffe ^{1*}, Christopher A-L. Jackson^{1,2}, Leonardo M. Pichel³

4 1. Basins Research Group (BRG), Department of Earth Science and Engineering, Imperial
5 College London, South Kensington Campus, SW7 2BP, UK

6 2. Jacobs, Manchester, M15 4GU, UK

7 3. Department of Earth Science, University of Bergen, Allégaten 41, 5007, Bergen,
8 Norway

9 **Abstract**

10 Salt tectonics is typically caused by the flow of mobile evaporites in response to post-
11 depositional gravity gliding and/or differential loading by overburden sediments. This situation
12 is considerably more complex near the margins of salt basins, where carbonate and clastic rocks
13 may be deposited at the same time and interbedded with more mobile evaporitic strata. In these
14 cases, syn-depositional salt flow may occur due to density differences in the deposited
15 lithologies, although our understanding of this and related processes is relatively poor. We here
16 use 3D seismic reflection and borehole data from the Devil's Hole Horst, West Central Shelf,
17 offshore UK to understand the genesis, geometry and kinematic evolution of intra-Zechstein
18 Supergroup (Lopingian) minibasins and their effect on post-depositional salt deformation. We
19 show that immobile, pinnacle-to-barrier-like, carbonate build-ups and anhydrite are largely
20 restricted to intra-basin highs, whereas mobile halite, which flowed to form large diapirs,
21 dominates in the deep basin. At the transition between the intra-basin highs and the dep basin,
22 a belt of intra-Zechstein minibasins occur, forming due to the subsidence of relatively dense
23 anhydrite into underlying halite. Depending on primary halite thickness, these intra-Zechstein

24 minibasins created topographic lows, dictating the position for nucleation and subsequent
25 down-building of Triassic minibasins. Our study refines the original depositional model for the
26 Zechstein Supergroup in the Central North Sea, with the results also helping us better
27 understand the style and distribution of syn-depositional salt flow on other layered evaporitic
28 sequences and the role intra-salt heterogeneity and related deformation may have in the
29 associated petroleum plays.

30 **Introduction**

31 Salt tectonics occurs in >100 sedimentary basins worldwide and is responsible for the
32 formation of a remarkably complex range of structures (see Jackson & Hudec, 2017). These
33 structures are important, given they can strongly influence the tectonostratigraphic evolution
34 and petroleum system development of these basins. Most studies focus on the structural styles
35 and stratigraphic patterns related to post-depositional salt flow; i.e. the post-depositional
36 mobilization of the salt in response to differential sediment loading, gravity gliding and/or
37 thick-skinned tectonics (Talbot & Jackson, 1987; Peel et al., 1996; Volozh et al., 2003; Hudec
38 and Jackson, 2004; Brun and Maunduit 2008, 2009; Quirk et al., 2012; Fernandez et al., 2017;
39 Pichel et al., 2018; Jackson et al., 2019). In these studies, the timing and style of salt flow is
40 typically recorded by deformation and stratigraphic patterns within the seismically well-
41 imaged, supra-salt sedimentary sequences (Jackson and Hudec, 2017). Conversely, much less
42 is known about the drivers and consequences of syn-depositional salt flow, for example how
43 the syn-depositional salt flow related to the primary lithology distribution within Layered
44 Evaporite Sequence (LES) (Rowan et al., 2019), what types of intra-salt structural styles form
45 because of this relatively early movement, or how syn-depositional movement impacts
46 subsequent post-depositional salt flow and related deformation. Our lack of knowledge of these
47 processes and their products possibly reflects the fact that evidence for syn-depositional salt
48 flow is often harder to obtain, given the difficulties associated with the seismic reflection

49 imaging of the internal (i.e. intra-salt) structure and stratigraphy of subsurface salt bodies (see
50 Jones and Davison, 2014). However, modern 3D seismic reflection data can occasionally image
51 intra-salt layering and complex intra-salt deformation patterns (e.g., Central North Sea,
52 offshore UK; Van Gent et al., 2011; Cartwright et al., 2012; e.g., Santos Basin, offshore Brazil;
53 Gamboa et al., 2008; Davison et al., 2012; Fiduk and Rowan, 2012; Dolley et al., 2015; Jackson
54 et al., 2015; Pichel et al., 2019; e.g., the Levant Basin; Gvirtzman et al., 2013). In some of these
55 examples, the relative timing between salt deposition and deformations is debatable, principally
56 due to intense post-depositional salt flow and diapirism obscuring the evidence of early-formed
57 intra-salt structures and stratigraphic patterns (i.e. thickness changes, onlaps) (Gamboa et al.,
58 2008; Davison et al., 2012; Dooley et al., 2015; Fiduk & Rowan, 2012).

59 In the Central North Sea, offshore eastern UK, syn-depositional salt flow was originally
60 described in the Zechstein Supergroup (Clark et al., 1998) (Figure 1). These authors show
61 several 2D seismic profiles characterising the seismic expression and structural style of intra-
62 Zechstein, syn-depositional minibasins, which they refer to as 'rafts'. Additionally, using
63 vintage 3D seismic reflection data they produce a series of thickness maps to illustrate how a
64 single intra-salt minibasin evolved, showing that the depocenter location was not fixed, but
65 instead shifted through time (Figure 1C, 1D). Several mechanisms were proposed by Clark et
66 al. (1998): (1) thin skinned extension triggered by basin-forming regional tilting; (2) syn-
67 Zechstein basement fault activation; (3) syn-Zechstein basement-induced shortening; (4)
68 differential loading created by shelf progradation; (5) gravity collapse due to density variations
69 between the halite/carbonate/anhydrite units; and (6) dissolution collapse. The authors
70 conclude these pre-Triassic, intra-Zechstein 'rafts', were most likely created by the
71 combination of two mechanisms: (i) thin-skinned extension which was triggered by regional
72 tilt; and (ii) sediment supply, which filled the accommodation created by the down-dip (i.e.,

73 basinward) flowing halite. How this behaviour related to the growth of adjacent salt structures
74 and subsidence patterns in nearby minibasins was not discussed.

75 Here we expand on these ideas initially formulated by Clark et al. (1998) by using modern, 3D
76 seismic reflection and borehole data from the eastern flank of the Devil's Hole Horst, UK
77 Central North Sea (Figure 1A). Our study area lie in a location characterised by marked spatial
78 changes in the lithology and overall thickness of the Zechstein Supergroup. This location,
79 coupled with minimal post-depositional deformation and high-resolution seismic imaging,
80 make the southern corner of the Devil's Hole Horst a prime location to revisit this under-
81 explored aspect of salt-tectonic (Figure 1A). By integrating 3D seismic reflection data and well
82 data, we can: (1) characterize and map syn-depositional, salt-related deformation within the
83 Zechstein Supergroup; (2) relate the structural style of syn-depositional minibasins to primary
84 lithology variations within the salt; and (3) explore how the syn-depositional salt flow
85 influenced post-depositional salt and overburden deformation.

86 **Geological Setting**

87 Cisuralian (Early Permian) rifting, associated with the development of the Central Graben,
88 influenced the location and extent of the Zechstein Supergroup evaporites (Ziegler, 1975;
89 Hodgson et al., 1992). During the early stages of rifting, subsidence rates exceeded sediment
90 accumulation rate, forming a sediment starved, intra-continental basin (Hodgson et al., 1992;
91 Glennie & Underhill, 1998). A marine transgression during the Guadalupian (Middle Permian)
92 resulted in desert lakes filling the rift-related relief, which when coupled with limited influx of
93 marine seawater, enabled the development of hyper-saline conditions and the deposition of an
94 evaporite-bearing sedimentary sequences (Smith, 1979; Ziegler, 1989; Glennie & Underhill,
95 1998; Taylor, 1998). More specifically, four to five cycles of flooding and evaporation during
96 the Lopingian (Late Permian) resulted in the deposition of a LES known as the Zechstein

97 Supergroup (Smith et al., 1993; Armour et al., 2004). Repeated flooding and evaporation
98 directly influenced lithology distribution in the Zechstein Supergroup, i.e., carbonate- and
99 anhydrite-rich units were deposited at the basin margins and on intra-basin structural highs
100 during highstands, whereas halite- and K-Mg-rich salt-rich units were deposited in the deeper
101 basins during lowstands (Tucker, 1991).

102 Based on the percentage of halite found in boreholes and inferred from salt-related structural
103 styles imaged in seismic reflection data, the Zechstein Supergroup is divided into four
104 depositional zones (DZ) (sensu Clark et al., 1998) (Figure 1A, 1B). DZ1 is located adjacent to
105 intra-basin structural highs, and consists mainly of shelfal carbonate, anhydrite, and clastic
106 rocks, with little or no halite (<10%). DZ2 is similar to DZ1 but contains a higher percentage
107 of halite (10-50%), whereas DZ3 is characterized by relatively minor amounts of shallow
108 waters shelfal rocks and a larger proportion of halite (50-80%). DZ2 and DZ3 together define
109 the transition from the basin margin to basin centre, they typically deposited on and thus define,
110 basinward-dipping slopes (Clark et al., 1998; Patruno et al., 2018; Grant et al., 2019; Jackson
111 et al., 2019). 3D seismic-based analysis of the Mid-North Sea High by Patruno et al. (2018)
112 indicate that this transitional region may be composed of a hybrid sulphate-carbonate platform
113 (termed Z1-2; following Taylor, 1998), capped by a thin, carbonate platform (termed Z3
114 following Taylor, 1998). Using the terminology of Clark et al. (1998), we would therefore
115 assign the Mid-North Sea High region to DZ1 or DZ2. Finally, the deep basinal areas are
116 defined by DZ4, which consists almost entirely of halite (>80%). In this zone diapirs and deep
117 minibasins represent the main salt-tectonic structures; in contrast, DZ1 and DZ2 are largely
118 undeformed or only weakly deformed due to the lack of mobile salt (Clark et al., 1998; Jackson
119 et al., 2019).

120 A second pulse of rifting during the Early Triassic reactivated the basement-involved, sub-salt
121 faults, triggering post-depositional flow and reactive rise of the overlying Zechstein

122 Supergroup salt (Jackson et al., 2019). In the halite-rich DZ3 and DZ4, stocks and N-trending
123 salt walls formed. Triassic salt tectonics resulted in relatively thick sequences of nonmarine
124 Triassic rocks being contained within minibasins; these sequences thin towards and onlap
125 flanking salt bodies (Ziegler, 1975). Later Jurassic rifting had limited effect on diapiric rise due
126 diapir welding, even if the extension could cause some diapiric collapse. Cretaceous and post-
127 Cretaceous post-rift shortening did not cause diapir rejuvenation on the basin flanks, only in t.
128 to did not impact salt-bearing structures who are the focus of this study.

129 **Data and Methodology**

130 We use a 1460 km² pre-stack time-migrated 3D seismic volume, that covers Zechstein
131 Supergroup DZ2- DZ4 (Figure 1). The seismic reflection data were shot in 2012 had processed
132 in 2014, which resulted in final bin-size of 12.5 x 12.5 m, a dominant frequency of 25 Hz at
133 depth of interest. The data is zero-phase processed with SEG ‘reverse’ polarity, where a
134 downward increase of acoustic impedance is represented by a negative (trough; blue) and
135 positive (peak; red) seismic reflection event, respectively. The dataset is in the NE portion of
136 Quadrant 28 on the United Kingdom Continental Shelf (UKCS), adjacent to areas in which
137 Clark et al. (1998) documented the syn-depositional flow and deformation of Zechstein
138 Supergroup salt (Figure 1A). Six wells were also available for this study; two wells are in DZ3
139 (28/9-4 & 28/4a) and four in DZ4. In our dataset, the lithology of DZ1 and DZ2 are not
140 constrained by wells and must thus be inferred from the prevailing salt-related structural style
141 (see Clark et al., 1998; Jackson et al., 2019). Two wells (28/4a-2 & 28/5-1) are only c. 10 km
142 apart, allowing us to constrain the boundary between DZ3 and DZ4 with relative precision
143 (Figure 1A).

144 We use well-logs to determine the current lithological variations within the Zechstein
145 Supergroup, given that post-depositional flow of the unit has undoubtedly modified the original

146 lateral and vertical (i.e., stratigraphic) distribution of the main rock types. More specifically, it
147 is likely that redistribution of the primary lithologies was rheologically controlled, with more
148 mobile halite and potash salt flowing more readily than less mobile clastic, anhydrite, and
149 carbonate rocks, such as those encountered at the base of the Zechstein Supergroup. (Jackson
150 et al., 2015). However, by considering: (i) the current lithological variability of the Zechstein
151 Supergroup in the context of its seismically imaged structural style and inferred kinematic
152 development; and (ii) other regional studies of the Zechstein Supergroup (Clark et al., 1998;
153 Jackson and Stewart, 2017; Jackson et al., 2019; Grant et al., 2019), we can infer the original
154 composition of the Zechstein Supergroup. Well data were also used to constrain the age of four
155 regional seismic horizons (base and top Zechstein, top Triassic, top Jurassic), and one intra-
156 salt horizon, which we mapped across the dataset (Figure 2). The base and top Zechstein
157 Supergroup reflections define the key salt-bearing interval, whereas the locally mappable intra-
158 salt reflection separates weakly reflective, halite-rich sequences below from more reflective,
159 halite-poor sequences above (see below). This distinction becomes important later when
160 discussing seismic-stratigraphic evidence for syn-depositional salt flow. Confidently
161 discriminate between syn- and post-Zechstein deformation, given salt-related deformation was
162 protracted, initially being driven by intra-Zechstein Supergroup density differences between
163 halite-anhydrite/carbonate, and then by evaporite-clastic differences in density between the
164 Zechstein Supergroup and Triassic, respectively. Notwithstanding this challenge, we define the
165 initial phase (i.e., syn-Zechstein Supergroup) of deformation by identifying intra-formational
166 onlaps and downlaps within the Zechstein Supergroup, between units with markedly different
167 seismic character. We then define the subsequent phase of deformation by identifying Triassic
168 onlap onto salt structures, in particular diapirs. Triassic minibasins are very weakly reflective,
169 whereas the overlying Jurassic interval is very reflective (Figure 3).

170 **Results**

171 Composition and Seismic Expression of the Zechstein Supergroup

172 We determined the composition of the Zechstein Supergroup using well-log data. Two wells
173 (28/4a-2 & 28/5-1) penetrated and logged the entirety of the Zechstein Supergroup, whereas
174 the other four penetrated and logged only its upper portion. The former two wells prove a 30-
175 50 m thick carbonate layer at the base of the otherwise evaporite-rich sequence (Figure 3). This
176 basal carbonate-rich unit characterises the Zechstein Supergroup across much of the North Sea,
177 recording the temporal transition from the non-marine environment recorded by the Rotliegend
178 Group to the more restrictive marine conditions in which the Zechstein was deposited (Glennie
179 & Underhill, 1998; Brackenridge et al., 2020). Well 28/5-1, which penetrates a diapir in DZ4
180 (c. 90% halite), shows an abrupt upward transition from the carbonate layer into a thick (650
181 m) halite interval, whereas the basal carbonate in well 28/4a-2 is separated from the overlying
182 halite unit (c. 60% of the total penetrated thickness) by a thin (c. 25 m), claystone-bearing unit.
183 In all wells the Zechstein Supergroup is capped by a 25-90 m thick anhydrite-dominated unit
184 that is locally interbedded with thin (5-10 m) layers of claystone (Figure 3). Based on its
185 apparent predominance to areas of inflated salt (i.e., diapir crests), we infer that this unit
186 represents crestal caprock formed by the preferential dissolution of halite and other soluble
187 rock types like potash salts, with the claystone possibly representing insoluble clastic material
188 that originally accumulated within the depositional sequence (e.g., Ulrich et al., 1984; Warren,
189 2006). Halite dominates the core of the underlying diapirs, as proven by 28/5-1 and 28/4a-2
190 (Figure 3).

191 Zechstein Supergroup Structural Framework

192 The base Zechstein surface has a convex-to-the-basin plan-view geometry that broadly dips
193 eastwards (Figure 4A). This convex shape reflects the study area's location on the eastern flank
194 of Devil's Hole Horst (Figure 1A). We also note that this shape mimics the boundaries between
195 the depositional zones mapped by Clark et al. (1998) (Figure 1A). The rest of the base Zechstein

196 surface is relatively smooth, dipping east, although an E-W striking, N-dipping fault occurs in
197 the north-eastern part of the dataset (Figure 4A). Other structures observed on the base
198 Zechstein surface are geometrically similar to those identified directly above on the top
199 Zechstein Supergroup surface (i.e., Figure 4A), suggesting they are geophysical artifacts
200 related to velocity pull-ups.

201 In a similar manner to the base Zechstein surface, the top Zechstein surface also dips eastwards.
202 The surface is, however, not smooth, but instead is defined by numerous salt diapirs, the most
203 prominent of which are two broadly curvilinear, sub-parallel, convex-into-the-basin salt walls
204 (SW1&SW2; Figure 4B&C). These walls are 1.5-7 km wide, 150-500 ms tall, and at least 30
205 km long, extending northwards and southwards outside of the dataset. SW1 has a very well-
206 defined, smooth margins but SW2 is more amorphous, being characterized by several W-
207 trending, spur-like walls that protrude from its eastern margin (Figure 4C). We observe shorter
208 protrusions, with a similar easterly trend, along the eastern edge of SW1. The salt walls are
209 separated by minibasins that are, between SW1 and SW2, broadly N-trending, elongate, and
210 convex-into-the-basin, like their bounding diapirs (MB2) (Figure 4C). The minibasin between
211 the margin and SW1 (MB1) dies-out north-eastwards as the flanking salt walls merge to form
212 a broader salt plateau (MB1; Figure 4C,). MB2 and other minibasins in the southerly portion
213 of SW2 contain isolated salt stocks that are 0.4-1.5 km in diameter and up to 500 ms tall
214 (Figures 4D, 6).

215 Intra-Zechstein Seismic Facies

216 We recognize four key seismic facies in the Zechstein Supergroup. The first is located mostly
217 in the west of our study area and is marked by a distinct, high-amplitude, positive (red)
218 reflection at the base of the Zechstein Supergroup, which define several broadly mounded
219 structures (Figure 7). The second is a seismically chaotic unit that is widespread at the base of
220 the Zechstein Supergroup, and which defines the core of the most prominent salt structures,

221 such as diapirs (Figures 5, 6). The third is defined by more continuous, moderate-amplitude
222 reflections that occur almost exclusively in upper part of the Zechstein Supergroup, and which
223 typically forms bowl-shaped packages that onlap and thin towards flanking diapirs (Figure 5,
224 7 – 9). Spatially, this seismic facies is restricted to the SE of the study area, mostly within DZ3
225 (as mapped by Clark et al. 1998) (Figure 1, 4E). The fourth seismic facies type is observed
226 locally at the top of the Zechstein Supergroup and is defined by moderate- to high-amplitude
227 reflections that onlap onto and/or dip away from broadly flat-topped diapirs (Figure 7B).

228 We interpret that the intra-salt reflectively and seismic facies changes in the Zechstein
229 Supergroup marks an upward transition from a halite-rich, diapiric unit (proven by wells 28/5-
230 1 and 28/4a-2; Fig. 2; cf., Jackson et al., 2015) to a more heterogeneous, anhydrite-dominated
231 unit (Rodriguez et al., 2018). Based on its bowl-shaped external form, and the fact that internal
232 reflections thin towards and onlap onto structures composed of the more chaotic seismic facies,
233 we interpret that intra-salt reflectivity in the upper part of the Zechstein Supergroup define
234 intra-salt minibasins, similar to those interpreted elsewhere in the Central North Sea (Clark et
235 al., 1998; Jackson and Steward, 2017). These intra-Zechstein minibasins are thinnest along the
236 westerly part of the study-area and within MB1, and thicker to the southeast (Figure 4E). We
237 also note that these minibasins may be perched along the flanks of the diapiric salt walls and,
238 occasionally, encased within the walls themselves (Figure 4F).

239 Intra-Zechstein Structural Framework

240 To better understand the types and possible origins of the different styles of intra-Zechstein
241 minibasins, we provide four examples of their structural and stratigraphic context using four
242 cross-sections trending broadly east, parallel to the structural dip of the base Zechstein (Figure
243 4B).

244 *Section 1*

245 The first cross-section is located within DZ2 and DZ3 and reveals several broadly mounded
246 structures at the base of the Zechstein (i.e., the first seismic facies) (Figure 7). These structures
247 are capped by a distinct high-amplitude positive (red) reflection that continue westwards,
248 towards the basin margin. The mounds form a series of approximately NNW-trending, 200-
249 300 m-wide, up to 200 ms-tall (i.e., up to 983 m-thick, based on the average interval velocity
250 of 4916 m/s extracted from the 28/5-1 sonic log), crescentic features (south in Figure 7B), or
251 lower-relief, more amorphous features (north in Figure 7B). These mounds are overlain by the
252 other three key seismic facies described above (i.e., halite-rich diapiric salt; deep pink in Figure
253 7A&C, an anhydrite-rich minibasin; light pink in Figure 7A&C, and carbonate rich units at the
254 base and top of the Zechstein Supergroup; light blue in Figure 7A&C). The second locally
255 onlaps the largest mounded structure at the base of the Zechstein Supergroup on the eastern
256 side of the section, with the third seismic facies type observed at the top of the Zechstein
257 Supergroup (Figure 7A). In the centre of the line, the diapir is the same height of and has similar
258 geometry to the other two diapirs but is associated with a soft (trough) blue reflection which
259 onlaps onto the western diapir, and is onlapped by the third seismic facies to the east.

260 Based on their mounded geometry and seismic expression (Figure 7C), the abundance of
261 carbonates at the base of the Zechstein Supergroup as demonstrated by wells (Figure 3), and
262 their tectono-stratigraphic context at the evaporitic basin margin, we interpret these base-
263 Zechstein features as carbonate build-ups (Figure 7A&C). These features are in an area
264 previously identified by Clark et al. (1998) as being carbonate-rich, further supporting our
265 interpretation. Similar carbonate-related features are documented in the Southern North Sea
266 (Grant et al., 2019). Given the description above, we infer these soft reflection at the top of the
267 central diapir are carbonate dominated, with the differences in the seismic expression between
268 the basal and top carbonate units (i.e., first and forth seismic facies) could be related to: (i) the

269 carbonates are lithologically and thus petrophysically distinct, thereby differing in terms of
270 their density and velocity; and/or (ii) the carbonate are lithologically and thus petrophysically
271 similar, but are overlain by different strata (e.g., Jurassic sandstone or mudstone) that define
272 either a downward increase in acoustic impedance and thus negative rather than positive, top-
273 salt reflection.

274 *Section 2*

275 The second cross-section is located mostly within DZ3. The most prominent features in this
276 section are the large, halite-rich diapirs (Figure 8). Small (150 ms tall by 1000 m wide),
277 triangular-shaped and generally more reflective bodies also occur locally at the base of the
278 Zechstein Supergroup. These bodies are overlapped and/or downlapped by highly reflective,
279 sigmoidal, clinoform-like reflections (Figure 8). These highly reflective sigmoidal reflections
280 are thickest adjacent to the large diapir to the east, overlapping its western flanks, forming an
281 asymmetric minibasin that is welded to the sub-salt strata (Figure 8B). Based on the more
282 pronounced thickness variations, truncations, and onlaps within the Zechstein Supergroup
283 relative to the Triassic minibasin which lies above, we infer that most of the salt flowed into
284 the diapir during the Permian, before Triassic deposition. However, salt continued to flow
285 during the Triassic, such that it affected thickness patterns in the lower parts of the minibasin
286 (Figure 8B). Where present, minor thickness variations in the Triassic minibasin mirror the
287 thickness variation in the intra-Zechstein packages (Figure 4E&H). We identify another
288 relatively small (200 ms thick), intra-salt minibasin in the centre of the cross-section (Figure
289 8A).

290 *Section 3*

291 The third cross-section shows two relatively thin (200-250 ms), bowl-shaped packages of semi-
292 continuous, intra-Zechstein reflections perched within a large salt wall (SW3; Figure 9A).
293 These packages thin towards and onlap onto flanking diapirs (Figure 9A). A similar, albeit

294 highly asymmetric sequence is also present dipping eastwards on the eastern flank of the large
295 wall and being overlain and indented by a small, Triassic minibasin (Figure 9A). Across the
296 section, Jurassic strata are broadly tabular and generally sub-horizontal, locally thinning across
297 and onlapping onto Triassic minibasins where these protrude above the top salt (Figure 9). We
298 suggest that the easterly dips within the easternmost intra-Zechstein minibasin was caused by
299 the subsequent subsidence of Triassic clastic strata down into the salt, which caused tilting of
300 the previous deposited evaporitic rocks (Figure 9B).

301 *Section 4*

302 Unlike the previous examples, the fourth and final example is in the southern part of the dataset
303 (Figure 4B). This area is characterised by higher density of intra-Zechstein minibasins, and
304 higher structural complexity (Figure 4E). In this example, two Triassic minibasins are present
305 (MB1 and MB2) and separated by two salt walls (SW1 and SW2) (Figure 5). The broad bowl-
306 shaped intra-Zechstein sequence below MB1 is relatively thin (150 ms), symmetrical in cross-
307 section (Figure 5) and elongate in map-view (Figure 4C). The intra-Zechstein minibasin below
308 MB2 is thickest on the flanks of SW2, thinning towards both the crest of the diapir and updip
309 towards the base of SW1. The Triassic minibasin MB2 is thickest where the intra-Zechstein
310 minibasin onlaps SW2 (Figure 5).

311 Based on thickness relationships between the intra-Zechstein minibasin below MB2 and the
312 Triassic minibasin, we interpret that the post-Zechstein subsidence of Triassic minibasins into
313 the underlying salt caused the intra-Zechstein minibasins to rotate south-eastwards (Figure 5B).
314 We generally observe more complex deformation in the southern part of the study area. In
315 particular, we see more evidence for tilting of intra-Zechstein minibasins due to the subsidence
316 of younger, Triassic minibasins. The reason for this is not clear, but it might reflect the fact that
317 in this region, down-flank of the Devil's Horse Horst, mobile halite was thicker and, therefore,

318 there was still material to be evacuated from below the intra-Zechstein minibasins when the
319 Triassic minibasins formed.

320 Triassic

321 The Triassic is mostly weakly reflection and chaotic, although it is locally defined by low-
322 amplitude, moderately continuous reflections. Where observed, these reflections/packages
323 define broadly isopachous intervals that may onlap the diapir flanks (Figures 5, 6, 8). The
324 relatively smooth (compared to the top-salt), regionally consistent eastward dip observed at the
325 top Triassic level (Figure 4E) indicates that salt-related deformation peaked during the
326 Lopingian-Early Triassic and declined during the Late Triassic-Early Jurassic. Other structures
327 superimposed on the general consistent eastward dip relate to continued salt flow during the
328 Triassic. Circular depressions are common, located above individual salt-stocks; these could
329 potentially be related to the dissolution of the crests of salt diapirs piercing this interval and/or
330 diapir collapse related to post-Triassic extension and diapir widening (Mannie et al., 2014).

331 **Interpretation and Discussion**

332 Syn-depositional salt-related deformation and controls on subsequent structural 333 style

334 Our 3D seismic reflection data from the eastern flank of the Devil's Hole Horst, UKCS, show
335 that the Zechstein Supergroup has a complex seismic-stratigraphic architecture. At the base of
336 the Zechstein Supergroup, well-data prove a basal carbonate build-up, which are also seen at
337 the seismic reflection data as mounded structures, and protruding carbonate platform (e.g.,
338 Figure 5 & 7). Semi-continuous, moderate-amplitude seismic reflection onlap and dip away
339 from weakly reflective, chaotic, sub-circular-to-elongate bodies. Well data also show that the
340 Zechstein Supergroup is lithologically heterogeneous, comprising of carbonate, halite, and
341 anhydrite. Based on these observations, we interpret that the reflective packages are intra-

342 Zechstein minibasins, whereas the chaotic bodies are diapirs. Although they are not penetrated
343 by wells, we infer that the minibasins are anhydrite-rich, whereas wells prove that the diapirs
344 comprise predominantly halite. Critically, the seismic-stratigraphic architecture of the
345 Zechstein Supergroup argues for pre-Triassic salt flow, adjacent to and/or overlying basal
346 carbonate build-ups. Similar observations and interpretations were made by Clark et al. (1998),
347 who originally mapped these features to the North and North-West of our study area.

348 We therefore argue that although the Zechstein Supergroup depositional model of Clark et al.
349 (1998) accurately captures the basin-scale distribution of the key rock types, because of its
350 more regional focus, and the data quality and quantity at that time, it does not demonstrate how
351 the variable density and mechanical properties of these rocks controlled syn- and post-
352 depositional salt flow and related deformation.

353 Here, we propose an update to the idealized model of Clark et al. (1998), by incorporating both
354 the structural and lithological variability observed within the Zechstein Supergroup in our
355 study-area (Figure 10). Our model envisages the same four main Zechstein Supergroup
356 depositional cycles and zones defined by Clark et al. (1998), with each cycle and zones
357 consisting of an initial carbonate deposition associated with marine transgression and basin
358 flooding, followed by the deposition of anhydrite, and then halite during basin desiccation.

359 Deposition during the first cycle (i.e., carbonate, anhydrite and then halite) occurs across the
360 generally smooth, basinward-dipping, base-Zechstein Supergroup surface. During this time,
361 there is no gravitational potential or significant vertical density variations to drive salt flow and
362 related deformation (Figure 10A). The second cycle starts with deposition of relatively dense
363 carbonate at the basin margin, on top of less dense halite (Figure 10A). The deposition of dense
364 carbonates and subsequent anhydrite on top of less dense and more mobile halite triggers down-
365 dip salt evacuation, inflation, and diapirism of the latter (Figure 10B). The second cycle ends

366 with the deposition of a second halite unit, coeval to the downdip flow, inflation and diapirism
367 of the previous halite unit (Figure 10C). The third cycle is also characterised by the deposition
368 of a basin-margin, carbonate-dominated unit (Figure 10D). Assuming the basinward flow of
369 halite during the preceding phases was sufficient to generate a local, salt-cored structural high,
370 the near-margin area may have been sufficiently shallow to allow the nucleation of shallow-
371 water carbonates (Figure 10D). This element of the model is supported by the first example
372 seen in Figure 7, which suggest that locally at least, carbonate build-ups could form on areas
373 of inflated, halite-rich salt, at some distance into the basin. The third cycle continues with
374 deposition of anhydrite (Figure 10E) followed by halite (Figure 10F). During deposition of
375 these evaporitic cycles, mobile halite deposited during previous cycles continued to flow down-
376 dip due to loading at the basin-margin by dense, carbonate-/anhydrite-rich units (Figure 10E,
377 10F). By the fourth cycle (Figure 10G), a progradational carbonate platform developed along
378 the basin margin, as observed in Figure 5, passing laterally basinward into anhydrite-rich
379 minibasins surrounded by halite-rich salt walls.

380 The variability of halite proportion in each cycle governs the magnitude and location of salt-
381 related deformation during Zechstein Supergroup deposition. The final halite thickness and
382 proportion in each cycle also influenced the style and intensity of post-depositional (i.e. post-
383 Lopingian) salt-related deformation (Figure 10H). In areas where the LES was halite-rich and
384 relatively thick, post-depositional salt flow was substantial, allowing large diapirs to form; in
385 contrast, in areas where the LES mobile halite was relatively thin and impure, post-depositional
386 deformation were less pronounced (Figure 4H). These differences in the magnitude of
387 deformation governed by the amount and proportion of halite in the different cycles, are seen
388 in our dataset, which result in the differences between the four cross-sections (Figures 7-9).
389 For example, carbonate deposition at the basin margin promoted the syn-depositional
390 basinward expulsion of mobile evaporites, favouring the development of larger Triassic

391 minibasins above the anhydrite-dominated intra-Zechstein minibasins, lateral to the
392 mechanically stronger carbonates (e.g., Figure 7). We also note that thickness changes in the
393 Triassic minibasins mirror those in the intra-Zechstein, suggesting that subtle topographic lows
394 above intra-Zechstein minibasins localised earliest Triassic deposition, thus triggering the
395 nucleation and dictating the position of the Triassic minibasins (e.g., Figure 4F&8).
396 Conversely, where intra-Zechstein minibasins were small relative to their flanking salt walls,
397 they did not act as nucleation sites for subsequent Triassic minibasins (e.g., Figure 9). Finally,
398 we show that thicker (and generally larger) intra-Zechstein minibasins are preferentially
399 formed where the mobile halite was initially thicker, in the deep basin (e.g., Figure 5).

400 In addition to being genetically related to the intra-Zechstein minibasins, the subsidence history
401 of the Triassic minibasins may have been controlled by the older structures. For example, the
402 Triassic minibasins contain strata units that are wedge- rather than bowl-shaped, which we
403 infer minibasin tilting during subsidence (e.g. Figure 5) (Rowan & Weimer, 1998; Jackson et
404 al., 2019). The reason for this is not clear, but it may reflect the fact that Triassic minibasins
405 impinged on the underlying Zechstein minibasin as they subsided, with the latter containing
406 relatively rigid, largely immobile anhydrite flanked by more mobile halite. Such similar
407 interactions between intra-salt and supra-salt were observed in the Precaspian Basin (Fernandez
408 et al., 2017), where encased intra-salt minibasins dip towards the supra-salt minibasins as a
409 consequent of loading by the younger minibasin strata (see Figures 12 and 15 in their text). As
410 such, our conceptual model may be more broadly applicable to other basin-margin and intra-
411 basin high positions in the Zechstein salt basin, as well as comparable locations in other global
412 salt basin containing layered evaporite sequences (see below).

413 Implications for understanding salt tectonics and petroleum systems in other salt
414 basins

415 The results of our study of Lopingian salt in the North Sea have more general, broader
416 implications for understanding salt tectonics and related petroleum systems development in
417 other salt basins. For example, in the Precaspian Basin, Kazakhstan, numerous, very large (up
418 to 3 km-thick), Permo-Triassic, syn-depositional, intra-salt minibasins are encased in thick,
419 Kungurian (Lower Permian) salt. Well data indicate that these intra-salt basins contain clastic,
420 carbonate, and evaporite (i.e., halite, anhydrite) rocks (Fernandez et al., 2017). The authors
421 suggest that the large proportion of relatively dense anhydrite and carbonate within these
422 minibasins was a key reason for their relatively quick encasement, confirming the importance
423 of vertical (i.e., stratigraphic) lithology and density variations in driving density-driven
424 subsidence. A notable difference between the North Sea and Precaspian examples is that in the
425 former case, syn-depositional minibasins were not encased, likely reflecting the fact they
426 nucleated above and subsided into an overall thinner, mobile, lower halite. Lateral (i.e., areal)
427 variations in lithology and thus density likely also play a key role in determining when and
428 where syn-depositional salt flow might occur. For example, in the North Sea and Precaspian
429 Basin, relatively early (i.e., syn-depositional) salt flow and tectonics occur towards the basin
430 margin in a transitional zone where mobile halite-rich sequences and denser, less-mobile halite-
431 poor sequences are interbedded (Tucker, 1991). We thus propose that early, syn-depositional,
432 sedimentary load-driven salt tectonics likely occurs in comparable settings in LES deposited
433 in other salt basins, i.e., in near-basin margin areas characterised by the most pronounced
434 lithological heterogeneity.

435 Syn-depositional salt flow within LES is documented in the Levant Basin, offshore Israel
436 (Gvirtzmann et al., 2013), and has been argued for in the Santos Basin, offshore Brazil
437 (Davison et al., 2012, Bose and Sullivan, 2022; see, however, a competing hypothesis presented

438 by Jackson et al., 2015). However, in these cases, early deformation and accommodation was
439 driven by gravity-gliding and contraction of the entire evaporite sequence, and not sediment
440 loading. Because of this, this style of early salt tectonics is not restricted to the basin margin
441 like the load-driven examples presented above but can instead occur anywhere within the basin
442 where contraction occurs (e.g., the distal part of a salt-detached passive margin or above a base-
443 salt step in a relatively proximal position; e.g., Dooley et al., 2016; Erdi and Jackson, 2021). In
444 addition, recent numerical models show that syn-depositional deformation can also occur
445 during the final stages of rifting, in a lithologically homogenous evaporite sequence lacking of
446 an intra-salt density difference. In this case, syn-depositional minibasin formation likely occurs
447 due to stretching-driven flow of salt (Pichel et al., 2022).

448 Regardless of the location in which it occurs and its origin, a key question is, therefore, “how
449 do we distinguish intra-salt structural styles and thickness changes related to syn-depositional
450 salt flow from those related to post-depositional deformation?” (see discussion in Allen et al.,
451 2016). Clearly, information on the regional geological context (e.g., to determine regional
452 events that may be responsible for driving salt tectonic-related deformation) and a combination
453 of high-quality 3D seismic and borehole data (e.g., to clearly image and lithologically
454 characterised the structures and stratigraphy of interest) are critical. For example, as suggested
455 above, is the study area in a near-margin location, and are relatively similar proportions of
456 halite-rich and halite-poor units encountered within the salt sequence? It is likely this
457 conditions are met in other salt basins, but that subsequent salt tectonics (e.g., the growth of
458 large diapirs and/or the formation of allochthonous salt bodies) meant that more subtle, earlier
459 formed structures, such as syn-depositional minibasins are structurally overprinted or cannot
460 be geophysically imaged. Our study area thus represents a “sweet-spot” within which these
461 geometries are not only preserved, most likely due to the relatively thin, lower, mobile halite,

462 but also imaged by seismic reflection data. Syn-depositional salt flow and early-formed
463 evaporite minibasins may be more common than currently thought.

464 The results of our study have implications for petroleum exploration, and hydrogen (H₂) and
465 carbon dioxide (CO₂) storage within the Southern North Sea and other salt basins. For example,
466 carbonates at various stratigraphic levels within the salt could represent reservoirs, as observed
467 in other parts of NW Europe (see review by Patruno et al., 2017), with syn-depositional
468 deformation driving trap formation, and overlying halite acting as a seal. Reservoir quality
469 within these units might vary downdip, with marginal grainstones passing basinward into rock
470 types of lower reservoir quality, such as wackestones.” Depending on their permeability,
471 extent, and connectivity these carbonates could, however, facilitate leakage of CO₂ stored in
472 underlying, Rotliegend Group clastics, and they may impact the geometry and volume of
473 caverns engineered to store H₂ (see review by Duffy et al., 2022).

474 **Conclusion**

475 We here used modern 3D seismic reflection and borehole data from the eastern flank of the
476 Devil’s Hole Horst, UK Central North Sea to provide seismic-stratigraphic evidence that
477 minibasin downbuilding and diapirism occurred during deposition of the Zechstein Supergroup
478 (i.e., syn-depositional salt tectonics). We show four examples of intra-salt minibasins,
479 characterised by different lithological variations and/or structural styles and discuss their
480 influence on syn-depositional salt flow and subsequent, post-depositional deformation. Our
481 first example shows how intra-Zechstein minibasins and halite-dominated diapirs develop
482 away from the mechanically stronger, carbonate-dominated Zechstein rocks. We then showed
483 how subtle topographic lows created by the intra-Zechstein minibasin control the nucleation of
484 post-depositional Triassic minibasins. Finally, we demonstrate that in places where halite was
485 still thick after the end of salt-deposition due to either (i) syn-depositional

486 mobilization/inflation or (ii) halite-rich deposition towards the deep-basin, post-depositional
487 minibasins were highly asymmetric. By integrating these observations, we propose a revised
488 kinematic-depositional model that correlates intra-Zechstein lithological variability with syn-
489 depositional salt deformation. We thus believe that our model is more broadly applicable to
490 other areas of the Zechstein salt basin than the one originally proposed by Clark et al. 1998.
491 Our model is also more applicable to layered evaporite sequences worldwide and may suggest
492 that syn-depositional deformation is likely a more common phenomenon than often observed
493 in areas affected by intense and long-lived post-depositional salt tectonics such as the Gulf of
494 Mexico and South Atlantic. The results of this work have implications for hydrocarbon
495 exploration and CO₂ sequestration in other salt basins, highlighting the structural and
496 stratigraphic complexity which may occur in sequences classically considered only as seals.

497 **Acknowledgments**

498 We would like to acknowledge TGS for permission to use the seismic reflection data shown in
499 this study, in particular Annette Flethøj Tvedten and Will King. We would also like to the
500 Schlumberger for their Petrel academic license to Imperial College London.

501 **References**

- 502 Allen, H., Jackson, C. A.-L., & Fraser, A. J. (2016). Gravity-driven deformation of a youthful
503 saline giant: the interplay between gliding and spreading in the Messinian basins of the
504 Eastern Mediterranean. *Petroleum Geoscience*, 22(4), 340–356.
505 <https://doi.org/10.1144/petgeo2016-034>
- 506 Armour, A., Evans, D., & Hickey, C. (2004). The Millennium Atlas : petroleum geology of
507 the central and northern North Sea THE MILLENNIUM ATLAS : of the Central and
508 The project to produce the Millennium Atlas was organised by : *Petroleum Geology*
- 509 Booth, J. R., Dean, M. C., DuVernay, A. E., & Styzen, M. J. (2003). Paleo-bathymetric controls
510 on the stratigraphic architecture and reservoir development of confined fans in the

- 511 Auger Basin: central Gulf of Mexico slope. *Marine and Petroleum Geology*, 20(6),
512 563–586. [https://doi.org/https://doi.org/10.1016/j.marpetgeo.2003.03.008](https://doi.org/10.1016/j.marpetgeo.2003.03.008)
- 513 Brackenridge, R. E., Underhill, J. R., Jamieson, R., & Bell, A. (2020). Structural and
514 stratigraphic evolution of the Mid North Sea High region of the UK Continental Shelf.
515 *Petroleum Geoscience*, 26(2), 154–173. <https://doi.org/10.1144/petgeo2019-076>
- 516 Brun, J. P., & Mauduit, T. P. O. (2008). Rollovers in salt tectonics: The inadequacy of the
517 listric fault model. *Tectonophysics*, 457(1–2), 1–11.
518 <https://doi.org/10.1016/j.tecto.2007.11.038>
- 519 Brun, J. P., & Mauduit, T. P. O. (2009). Salt rollers: Structure and kinematics from analogue
520 modelling. *Marine and Petroleum Geology*, 26(2), 249–258.
521 <https://doi.org/10.1016/j.marpetgeo.2008.02.002>
- 522 Cartwright, J., Jackson, M., Dooley, T., & Higgins, S. (2012). Strain partitioning in gravity-
523 driven shortening of a thick, multilayered evaporite sequence. *Geological Society*
524 *Special Publication*, 363(1), 449–470. <https://doi.org/10.1144/SP363.21>
- 525 Clark, J. A., Stewart, S. A., & Cartwright, J. A. (1998). Evolution of the NW margin of the
526 North Permian Basin, UK North Sea. *Journal of the Geological Society*, 155(4), 663.
527 <https://doi.org/10.1144/gsjgs.155.4.0663>
- 528 Davison, I., Anderson, L., & Nuttall, P. (2012). Salt deposition, loading and gravity drainage
529 in the Campos and Santos salt basins. *Geological Society, London, Special*
530 *Publications*, 363(1), 159 LP – 174. <https://doi.org/10.1144/SP363.8>
- 531 Dooley, T. P., Jackson, M. P. A., Jackson, C. A. L., Hudec, M. R., & Rodriguez, C. R. (2015).
532 Enigmatic structures within salt walls of the Santos Basin-Part 2: Mechanical
533 explanation from physical modelling. *Journal of Structural Geology*, 75, 163–187.
534 <https://doi.org/10.1016/j.jsg.2015.01.009>
- 535 Fernandez, N., Duffy, O. B., Hudec, M. R., Jackson, M. P. A., Burg, G., Jackson, C. A. L., &
536 Dooley, T. P. (2017). The origin of salt-encased sediment packages: Observations from
537 the SE Precaspian Basin (Kazakhstan). *Journal of Structural Geology*, 97, 237–256.
538 <https://doi.org/10.1016/j.jsg.2017.01.008>

- 539 Fiduk, J. C., & Rowan, M. G. (2012). Analysis of folding and deformation within layered
540 evaporites in blocks BM-S-8 & -9, Santos Basin, Brazil. *Geological Society Special*
541 *Publication*, 363(1), 471–487. <https://doi.org/10.1144/SP363.22>
- 542 Gamboa, L. A. P., Machado, M. A. P., Da Silveira, D. P., De Freitas, J. T. R., Da Silva, S. R.
543 P., Mohriak, W., Szatmari, P., & ANJOS, S. (2008). Evaporitos estratificados no
544 Atlântico Sul: interpretação sísmica e controle tectono-estratigráfico na Bacia de
545 Santos. *Sal: Geologia e Tectônica, Exemplos Nas Basicas Brasileiras*, 340–359.
- 546 Glennie, K. W., & Underhill, J. R. (1998). Origin, Development and Evolution of Structural
547 Styles. In *Petroleum Geology of the North Sea* (pp. 42–84).
548 <https://doi.org/https://doi.org/10.1002/9781444313413.ch2>
- 549 Grant, R. J., Underhill, J. R., Hernández-Casado, J., Barker, S. M., & Jamieson, R. J. (2019).
550 Upper Permian Zechstein Supergroup carbonate-evaporite platform palaeomorphology
551 in the UK Southern North Sea. *Marine and Petroleum Geology*, 100, 484–518.
552 <https://doi.org/10.1016/j.marpetgeo.2017.11.029>
- 553 Gvirtzman, Z., Reshef, M., Buch-Leviatan, O., & Ben-Avraham, Z. (2013). Intense salt
554 deformation in the Levant Basin in the middle of the Messinian Salinity Crisis. *Earth*
555 *and Planetary Science Letters*, 379, 108–119.
556 <https://doi.org/10.1016/j.epsl.2013.07.018>
- 557 Hodgson, N. A., Farnsworth, J., & Fraser, A. J. (1992). Salt-related tectonics, sedimentation
558 and hydrocarbon plays in the Central Graben, North Sea, UKCS. *Geological Society,*
559 *London, Special Publications*, 67(1), 31 LP – 63.
560 <https://doi.org/10.1144/GSL.SP.1992.067.01.03>
- 561 Hudec, M. R., & Jackson, M. P. A. (2004). Regional restoration across the Kwanza Basin,
562 Angola: Salt tectonics triggered by repeated uplift of a metastable passive margin.
563 *AAPG Bulletin*, v, 88(7), 971–990. <https://doi.org/10.1306/02050403061>
- 564 Jackson, C. A. L., Jackson, M. P. A., & Hudec, M. R. (2015). Understanding the kinematics of
565 salt-bearing passive margins: A critical test of competing hypotheses for the origin of
566 the Albian Gap, Santos Basin, offshore Brazil. *Bulletin of the Geological Society of*
567 *America*, 127(11–12), 1730–1751. <https://doi.org/10.1130/B31290.1>

- 568 Jackson, C. A. L., Jackson, M. P. A., Hudec, M. R., & Rodriguez, C. R. (2015). Enigmatic
569 structures within salt walls of the Santos Basin-Part 1: Geometry and kinematics from
570 3D seismic reflection and well data. *Journal of Structural Geology*, 75, 135–162.
571 <https://doi.org/10.1016/j.jsg.2015.01.010>
- 572 Jackson, C. A.-L., Duffy, O. B., Fernandez, N., Dooley, T. P., Hudec, M. R., Jackson, M. P.
573 A., & Burg, G. (2019). The stratigraphic record of minibasin subsidence, Precaspian
574 Basin, Kazakhstan. *Basin Research*, 0(0), 1–25. <https://doi.org/10.1111/bre.12393>
- 575 Jackson, C. A.-L., & Stewart, S. A. (2017). Composition, Tectonics, and Hydrocarbon
576 Significance of Zechstein Supergroup Salt on the United Kingdom and Norwegian
577 Continental Shelves: A Review. *Permo-Triassic Salt Provinces of Europe, North Africa
578 and the Atlantic Margins*, 175–201. [https://doi.org/10.1016/B978-0-12-809417-
579 4.00009-4](https://doi.org/10.1016/B978-0-12-809417-4.00009-4)
- 580 Jackson, C., Elliott, G. M., Royce-Rogers, E., Gawthorpe, R. L., & Aas, T. E. (2019). Salt
581 thickness and composition influence rift structural style, northern North Sea, offshore
582 Norway. *Basin Research*, 31(3), 514–538. <https://doi.org/10.1111/bre.12332>
- 583 Jackson, M. P. A., & Hudec, M. R. (Eds.). (2017). Salt Tectonics. In *Salt Tectonics: Principles
584 and Practice*. Cambridge University Press. <https://doi.org/DOI: undefined>
- 585 Jones, I. F., & Davison, I. (2014). Seismic imaging in and around salt bodies. *Interpretation*,
586 2(4), SL1–SL20. <https://doi.org/10.1190/INT-2014-0033.1>
- 587 Mannie, A. S., Jackson, C. A.-L., & Hampson, G. J. (2014). Shallow-marine reservoir
588 development in extensional diapir-collapse minibasins: An integrated subsurface case
589 study from the Upper Jurassic of the Cod terrace, Norwegian North Sea. *AAPG Bulletin*,
590 98(10), 2019–2055. <https://doi.org/10.1306/03201413161>
- 591 Patruno, S., Reid, W., Jackson, C. A.-L., & Davies, C. (2018). New insights into the
592 unexploited reservoir potential of the Mid North Sea High (UKCS quadrants 35–38 and
593 41–43): a newly described intra-Zechstein sulphate–carbonate platform complex.
594 *Geological Society, London, Petroleum Geology Conference Series*, 8(1), 87.
595 <https://doi.org/10.1144/PGC8.9>

- 596 Peel, F. J., Travis, C., & Hossack, J. (1996). Genetic structural provinces and salt tectonics of
597 the Cenozoic offshore US Gulf of Mexico: A preliminary analysis. *AAPG Memoir*, 65,
598 153–175.
- 599 Pichel, L. M., Finch, E., & Gawthorpe, R. L. (2019). The Impact of Pre-Salt Rift Topography
600 on Salt Tectonics: A Discrete-Element Modeling Approach. *Tectonics*, 38(4), 1466–
601 1488. <https://doi.org/10.1029/2018TC005174>
- 602 Pichel, L. M., Peel, F., Jackson, C. A.-L., & Huuse, M. (2018). Geometry and kinematics of
603 salt-detached ramp syncline basins. *Journal of Structural Geology*, 115, 208–230.
604 <https://doi.org/https://doi.org/10.1016/j.jsg.2018.07.016>
- 605 Quirk, D. G., Schødt, N., Lassen, B., Ings, S. J., Hsu, D., Hirsch, K. K., & Von Nicolai, C.
606 (2012). Salt tectonics on passive margins: examples from Santos, Campos and Kwanza
607 basins. *Geological Society, London, Special Publications*, 363(1), 207–244.
608 <https://doi.org/10.1144/sp363.10>
- 609 Rodriguez, C. R., Jackson, A.-L., Rotevatn, A., Bell, R. E., & Francis, M. (2018). Dual
610 tectonic-climatic controls on salt giant deposition in the Santos Basin. *Brazil*
611 *GEOSPHERE* |, 14(1). <https://doi.org/10.1130/GES01434.1>
- 612 Rowan, M. G., Urai, J. L., Carl Fiduk, J., & Kukla, P. A. (2019). Deformation of intrasalt
613 competent layers in different modes of salt tectonics. *Solid Earth*, 10(3), 987–1013.
614 <https://doi.org/10.5194/SE-10-987-2019>
- 615 Rowan, M. G., & Weimer, P. (1998). Salt-sediment interaction, northern Green Canyon and
616 Ewing Bank (offshore Louisiana), northern Gulf of Mexico. *AAPG Bulletin*, 82(5B),
617 1055–1082.
- 618 Smith, D. B. (1979). Rapid marine transgressions and regressions of the Upper Permian
619 Zechstein Sea. *Journal of the Geological Society*, 136(2), 155 LP – 156.
620 <https://doi.org/10.1144/gsjgs.136.2.0155>
- 621 Smith, R. I., Hodgson, N., & Fulton, M. (1993). Salt control on Triassic reservoir distribution,
622 UKCS Central North Sea. *Geological Society, London, Petroleum Geology Conference*
623 *Series*, 4(1), 547 LP – 557. <https://doi.org/10.1144/0040547>
- 624 Talbot, C. J., & Jackson, M. P. A. (1987). SALT TECTONICS. *Scientific American*, 257(2),
625 70–79. <https://doi.org/10.1038/scientificamerican0887-70>

- 626 Taylor, J. C. M. (1998). Upper Permian—Zechstein. In *Petroleum Geology of the North Sea*
627 (pp. 174–211). <https://doi.org/https://doi.org/10.1002/9781444313413.ch6>
- 628 Tucker, M. E. (1991). Sequence stratigraphy of carbonate-evaporite basins: models and
629 application to the Upper Permian (Zechstein) of northeast England and adjoining North
630 Sea. *Journal of the Geological Society*, 148(6), 1019 LP – 1036.
631 <https://doi.org/10.1144/gsjgs.148.6.1019>
- 632 Ulrich, M. R., Kyle, J. R., & Price, P. E. (1984). Metallic sulfide deposits in the Winnfield salt
633 dome, Louisiana: evidence for episodic introduction of metalliferous brines during cap
634 rock formation. In *Transactions, Gulf Coast Association of Geological Societies* (Vol.
635 34, pp. 435–422). GCAGS Transactions. <https://doi.org/10.1306/ad4618b3-16f7-11d7-8645000102c1865d>
- 637 Van Gent, H., Urai, J. L., & de Keijzer, M. (2011). The internal geometry of salt structures - A
638 first look using 3D seismic data from the Zechstein of the Netherlands. *Journal of*
639 *Structural Geology*, 33(3), 292–311. <https://doi.org/10.1016/j.jsg.2010.07.005>
- 640 Volozh, Y., Talbot, C., & Ismail-Zadeh, A. (2003). Salt structures and hydrocarbons in the
641 Pricaspian basin. *American Association of Petroleum Geologists Bulletin*, 87(2), 313–
642 334. <https://doi.org/10.1306/09060200896>
- 643 Warren, J. K. (2006). Evaporites: Sediments, resources and hydrocarbons. In *Evaporites:*
644 *Sediments, Resources and Hydrocarbons*. <https://doi.org/10.1007/3-540-32344-9>
- 645 Ziegler, M. A. (1989). North German Zechstein facies patterns in relation to their substrate.
646 *International Journal of Earth Sciences : Geologische Rundschau*, 78(1), 105–127.
647 <https://doi.org/10.1007/BF01988356>
- 648 Ziegler, P. A. (1975). Geologic Evolution of North Sea and Its Tectonic Framework1. *AAPG*
649 *Bulletin*, 59(7), 1073–1097. <https://doi.org/10.1306/83D91F2E-16C7-11D7-8645000102C1865D>

651 **Figure Captions**

652 Figure 1: (A) Map showing the different depositional zones of the Zechstein Supergroup within
653 the Central North Sea, as described by Clark et al., 1998. Highlighted are the 3D seismic
654 surveys available for Clark et al., 1998 study and this study (zoomed area). Notice the dataset

655 is located outside of the zone of syn-depositional salt flow as described by Clark et al., 1998.
656 (B) Schematic cross-section describing an idealized deposition sequence of the Zechstein
657 Supergroup through X-X' in A. (C) Cross-section through the one intra-Zechstein minibasin
658 which was described in 3D by Clark et al. (1998). (D) Thickness maps of the sequences
659 described in C are evidence for syn-depositional salt flow in the Zechstein Supergroup
660 (Modified from Clark et al. (1998)).

661 Figure 2: Seismic well-tie for the 28/5a-2 well. We cannot fully constrain the intra-Zechstein
662 minibasins lithology as no wells penetrated the intra-Zechstein minibasins in our dataset. This
663 seismic well-tie holds the basis to the interpretation of our regional, supra-salt, horizons.

664 Figure 3: Well correlation panel through 5 of the 6 available wells flattened on Top Zechstein
665 (for location see Figure 1A). Wells 28/4a-2 & 28/5-1 had penetrated and logged the entirety of
666 the Zechstein Supergroup whereas the other four had logged only the upper portion of the
667 Zechstein Supergroup. The former two wells prove a 30-50 m thick carbonate layers at the base
668 of the otherwise evaporite-rich sequence. All wells show the presence of anhydrite and/or
669 layered sequences of sedimentary facies at the top of the Zechstein Supergroup.

670 Figure 4: (A) Base-Zechstein Super Group structural map. A significant convex-to-basin shape
671 is probably associated by the location relative to the Devil's Hole Horst (see Figure 1A for
672 location). (B) Structural map of the top Zechstein Supergroup. Same curvilinear convex-to-
673 basin is present, demonstrated by the salt walls architecture. (C) Location of the various salt
674 walls (SW) and minibasins (MB) overlain on the top - Zechstein Supergroup structural map for
675 orientation. (D) Red circles indicate isolated salt stocks located within MB2 and beyond SW3,
676 with few are located within SW3 (E) Thickness map of the intra-Zechstein minibasins,
677 overlaid on a grey-scale Top Zechstein structural map. (F) Halite Thickness map, location of
678 the intra-Zechstein (in Yellow) overlaid. (E) Top Triassic structural map not showing any
679 clear indication for the curvilinear structures. (H) Triassic thickness map.

680 Figure 5: NW-SE trending seismic (above) and Geoseismic (below) profiles through the
681 southern part of the dataset. Visible is the carbonate dominated margin of the Devil's Horst
682 Hole (SW1). At the centre of the figure, a large Triassic minibasin caused the rotation of the
683 intra-Zechstein minibasin. For location see Figure 3D.

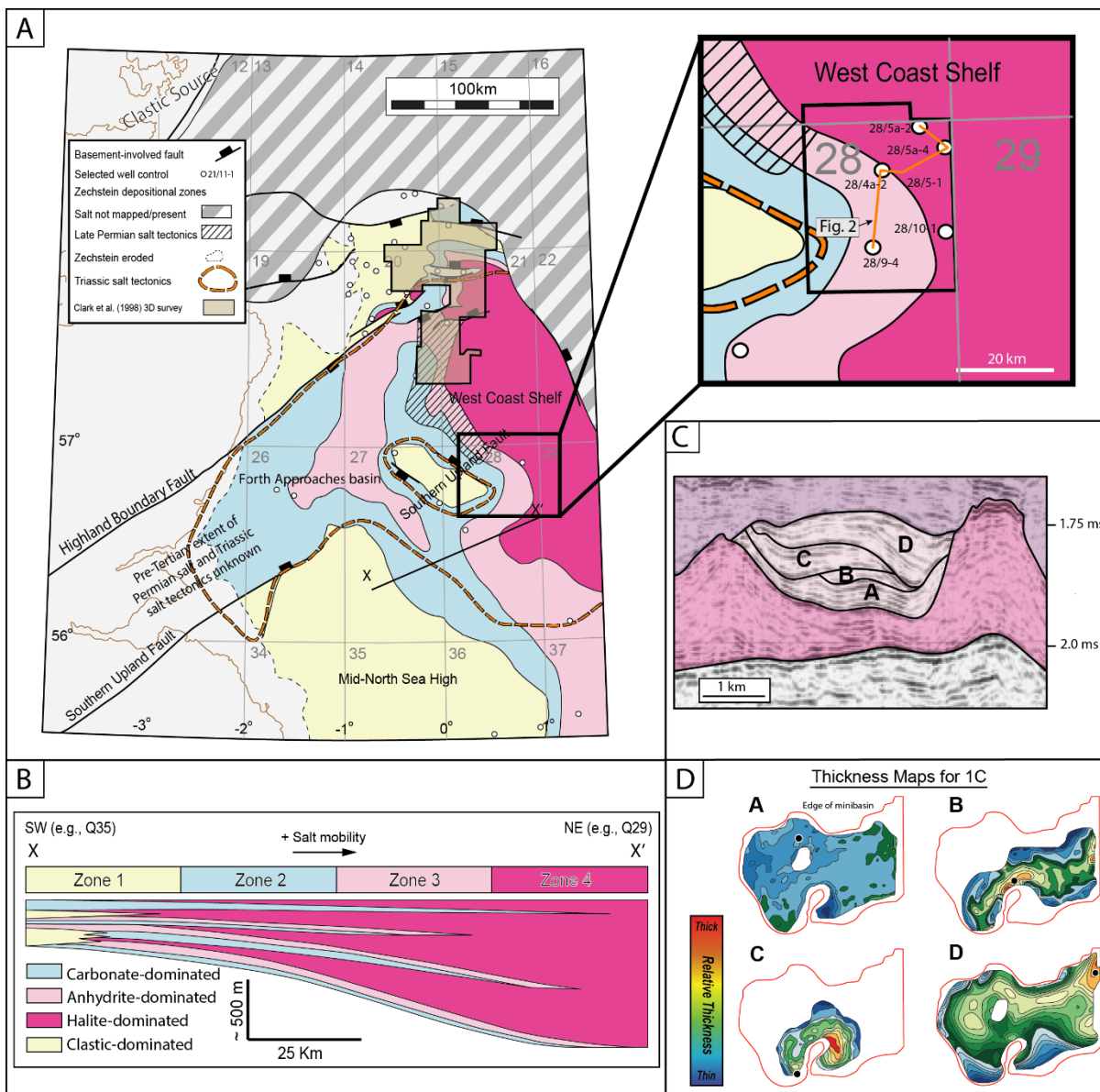
684 Figure 6: Seismic cross section along the centre of MB2. Isolated salt stocks are trapped within
685 the curvilinear minibasin. Intra-Zechstein reflection are also highlighted. For location see
686 Figure 4B.

687 Figure 7: (A) W-E trending seismic and Geoseismic profiles through a carbonate-halite
688 dominated intra-Zechstein minibasins. For location see Figure 3D. (B) Map of the top
689 carbonate-rich interval at the base of the Zechstein Supergroup. (C) N-S trending seismic
690 (above) and Geoseismic (below) profile through the carbonate-rich base-Zechstein buildups
691 (for location see Figure 7B).

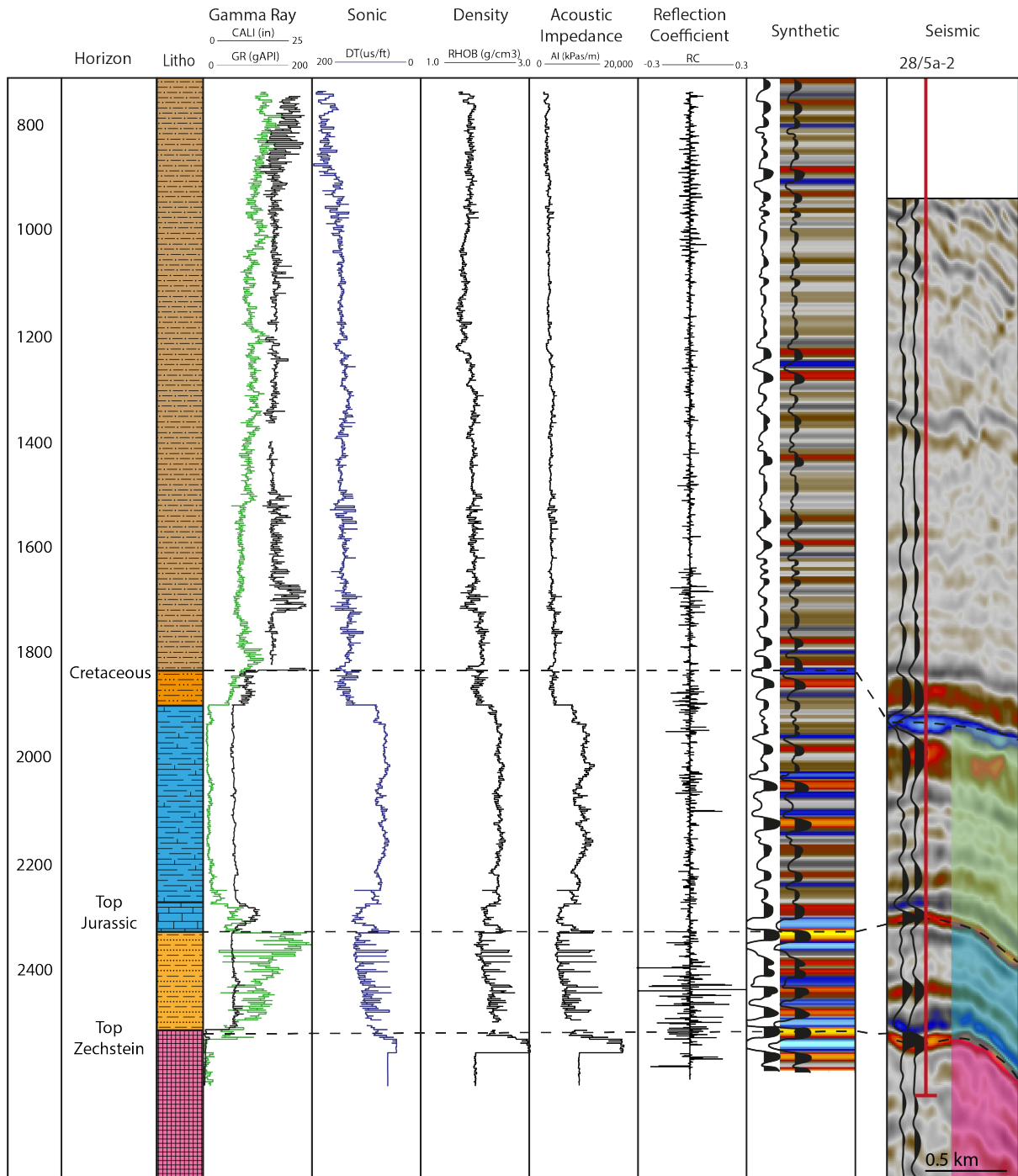
692 Figure 8: W-E trending seismic (above) and Geoseismic (below) profiles through the
693 anhydrite-halite dominated intra-Zechstein minibasins. For location see Figure 3D.

694 Figure 9: W-E trending seismic (above) and Geoseismic (below) profiles through SW3
695 showing two symmetrical minibasins in its centre. For location see Figure 3D.

696 Figure 10: A revised depositional model for the Zechstein Supergroup along the eastern flank
697 of Devil's Hole Horst showing the different phases of syn-depositional salt flow.

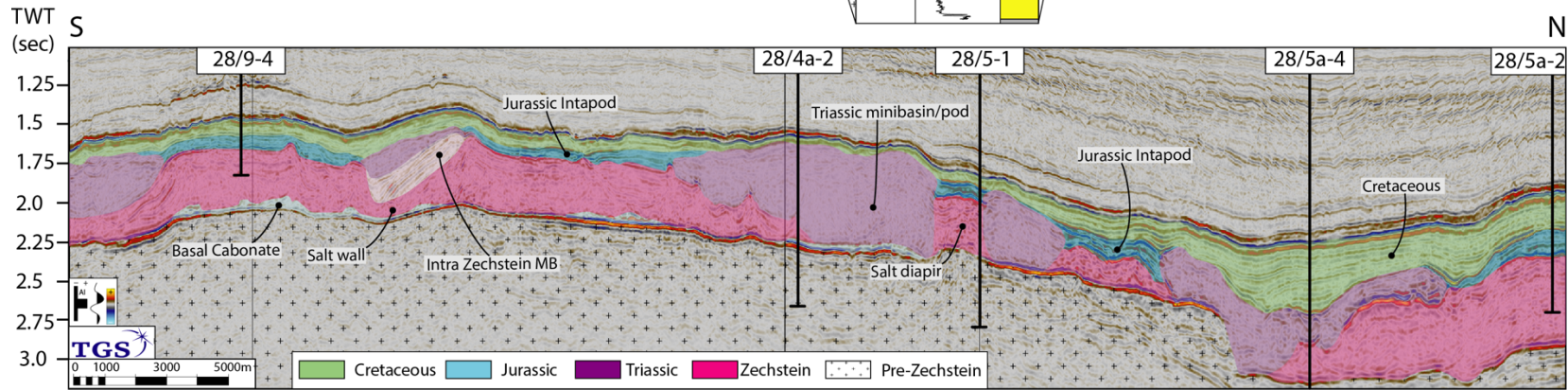
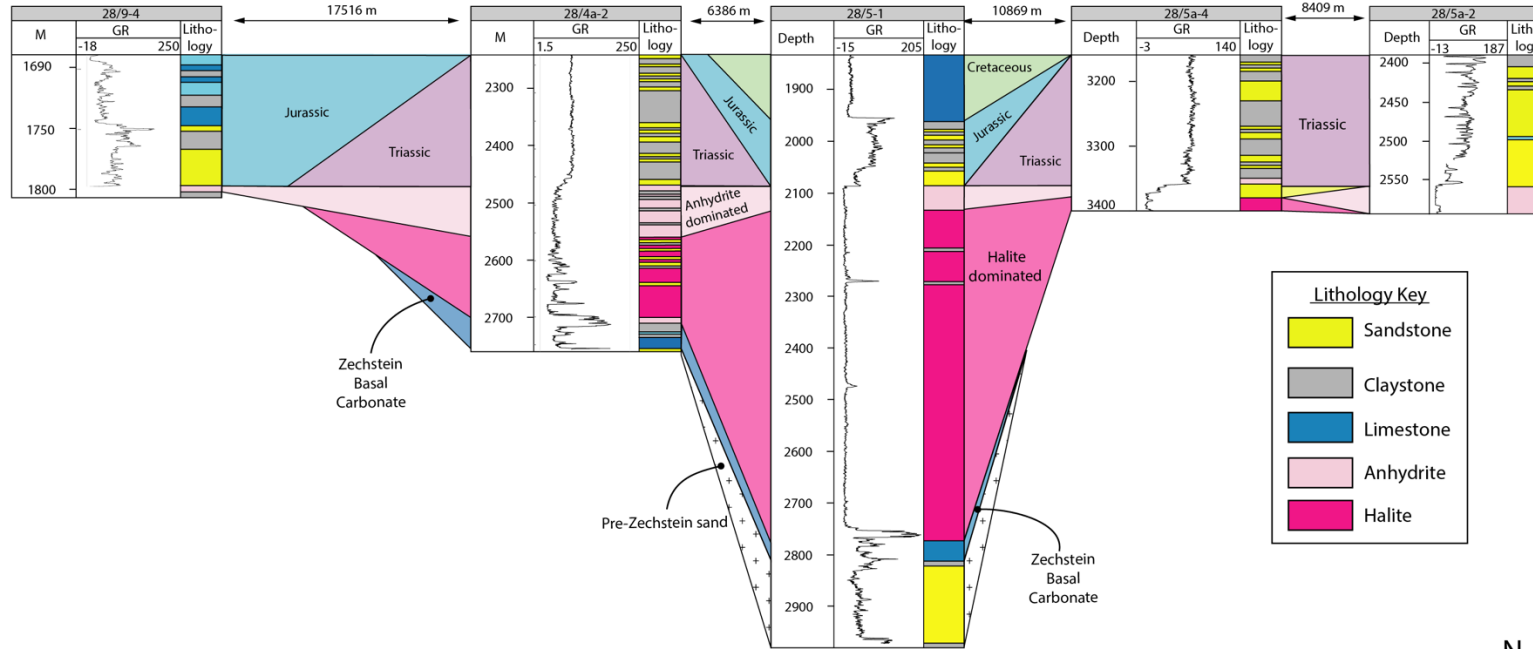


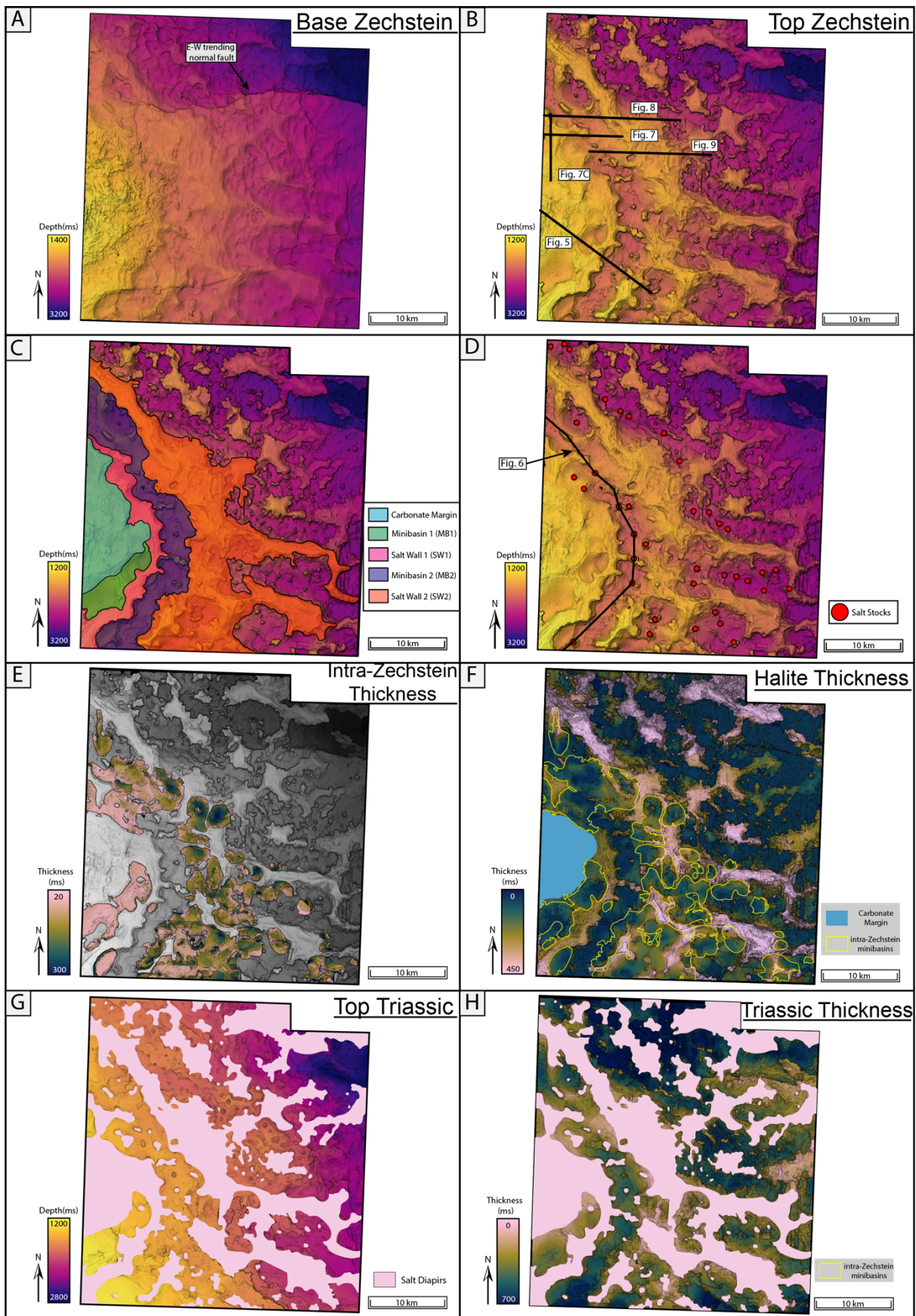
702 Figure 2

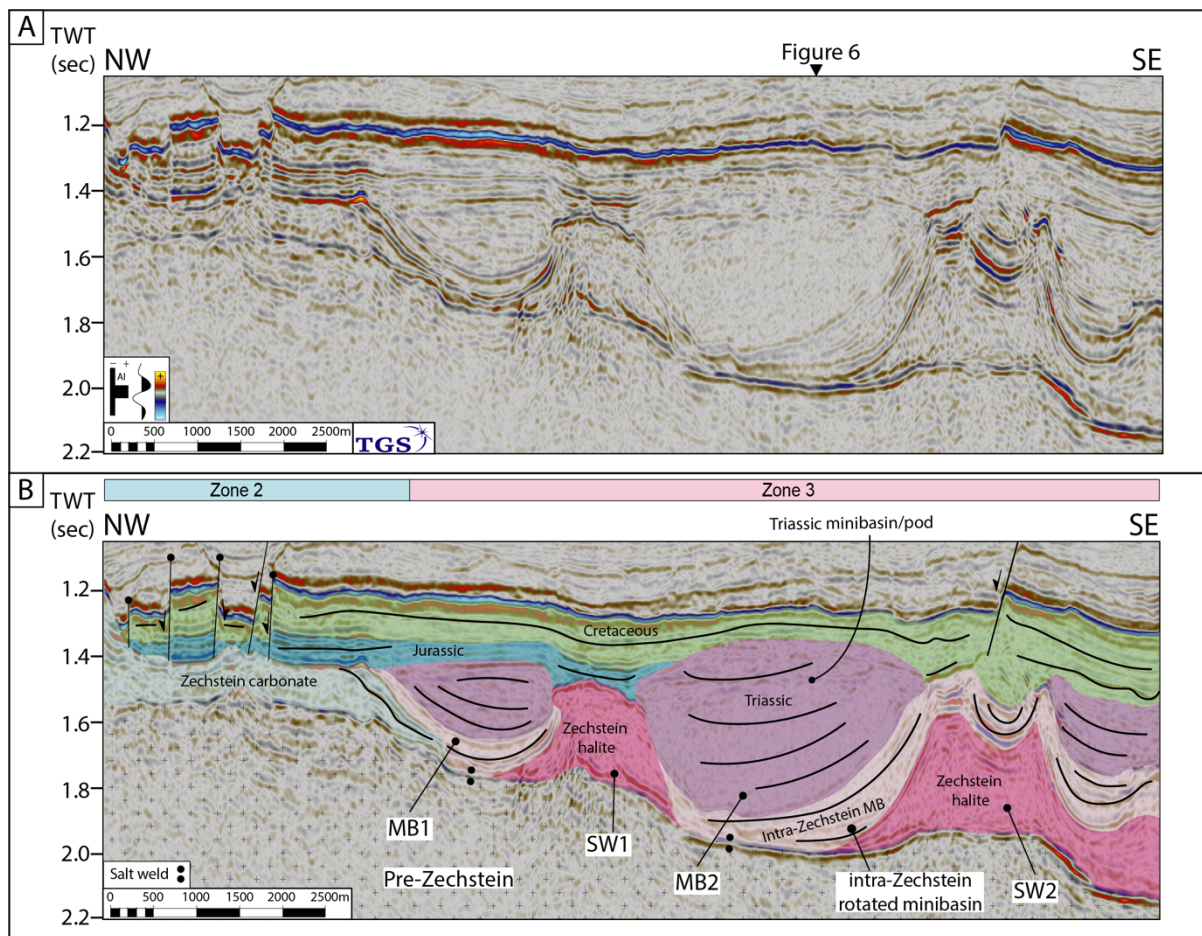


703

704 Figure 3



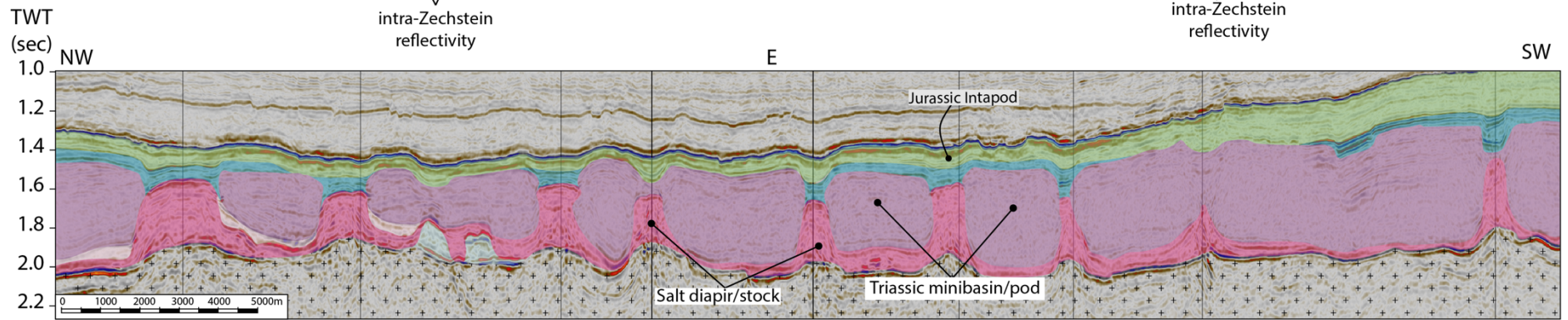
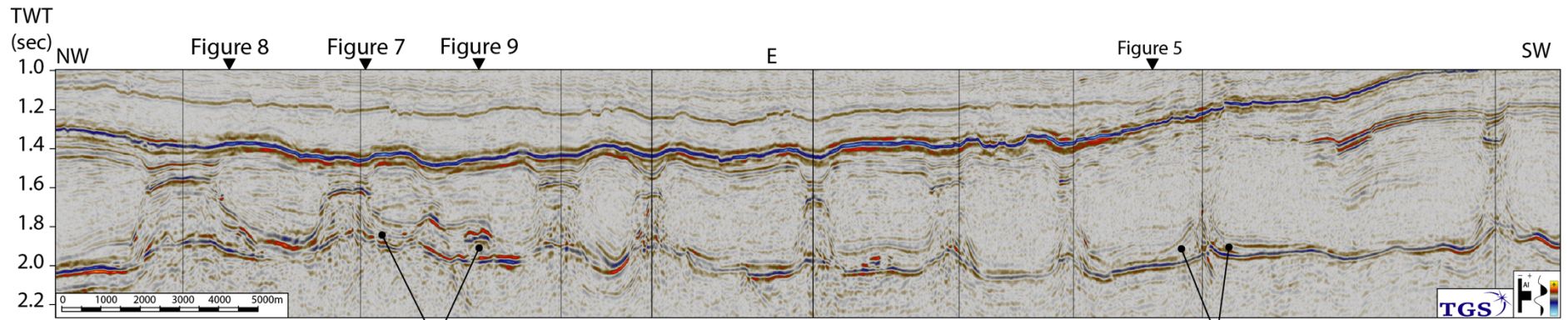




709

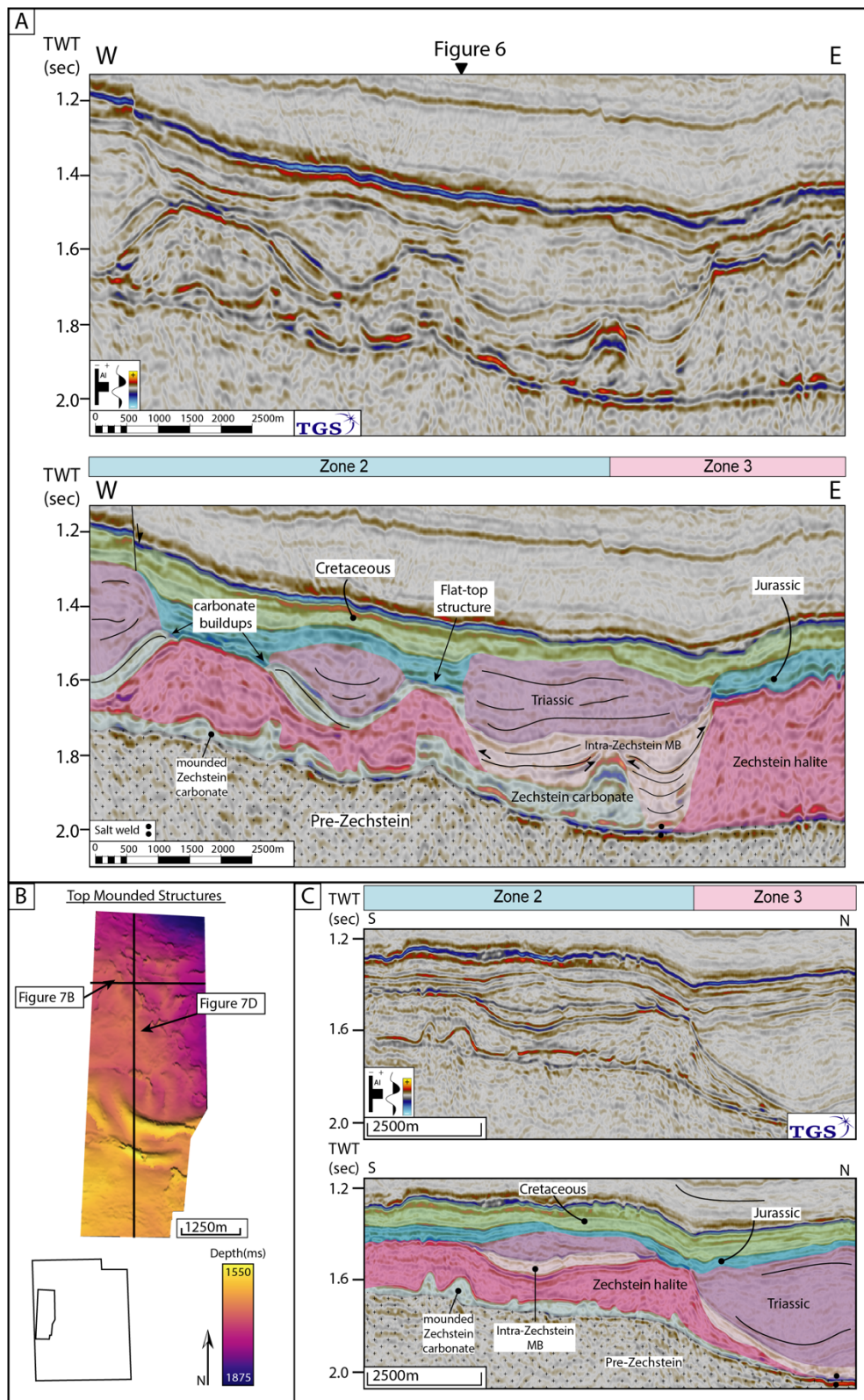
710

711 Figure 6

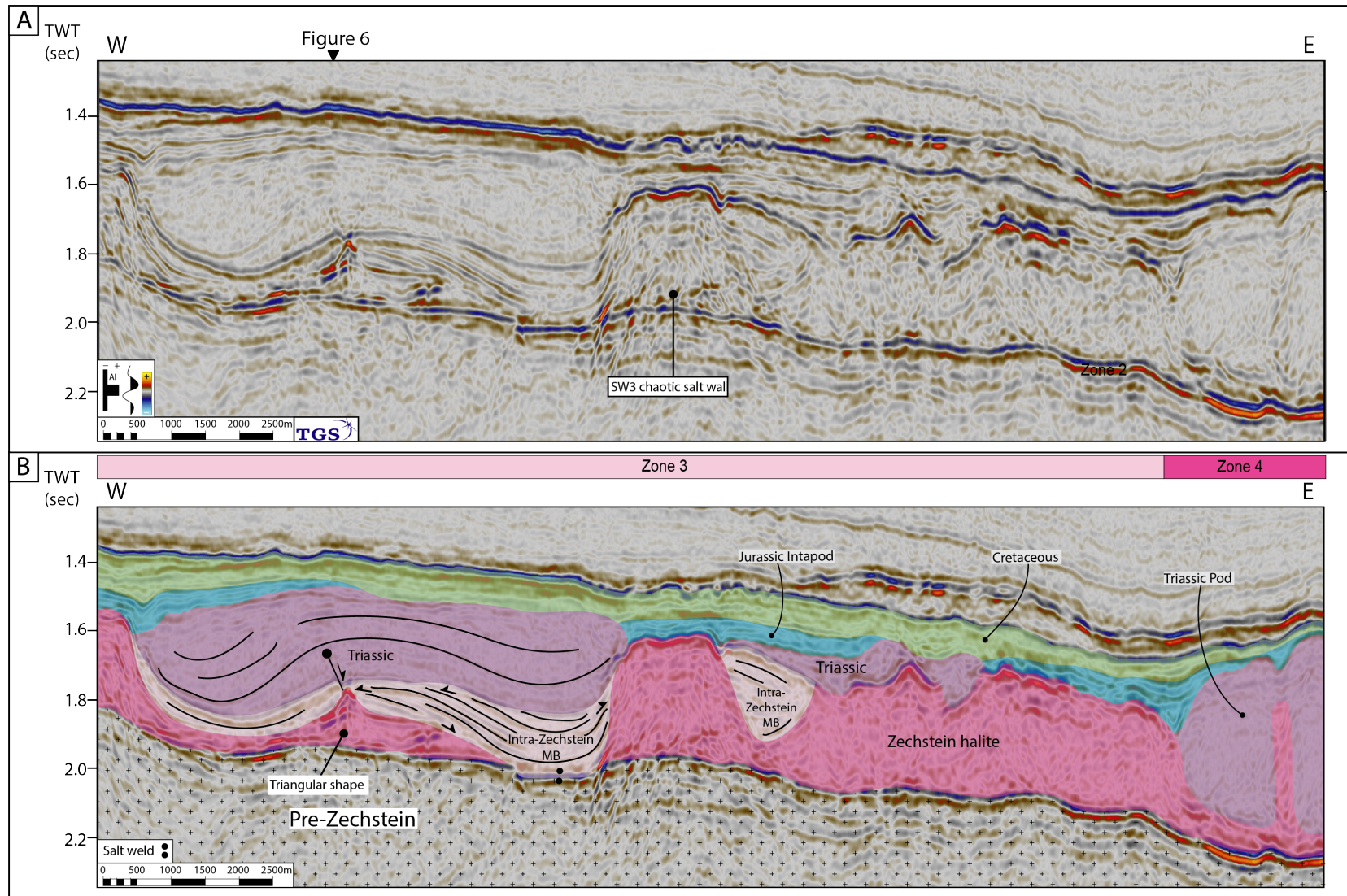


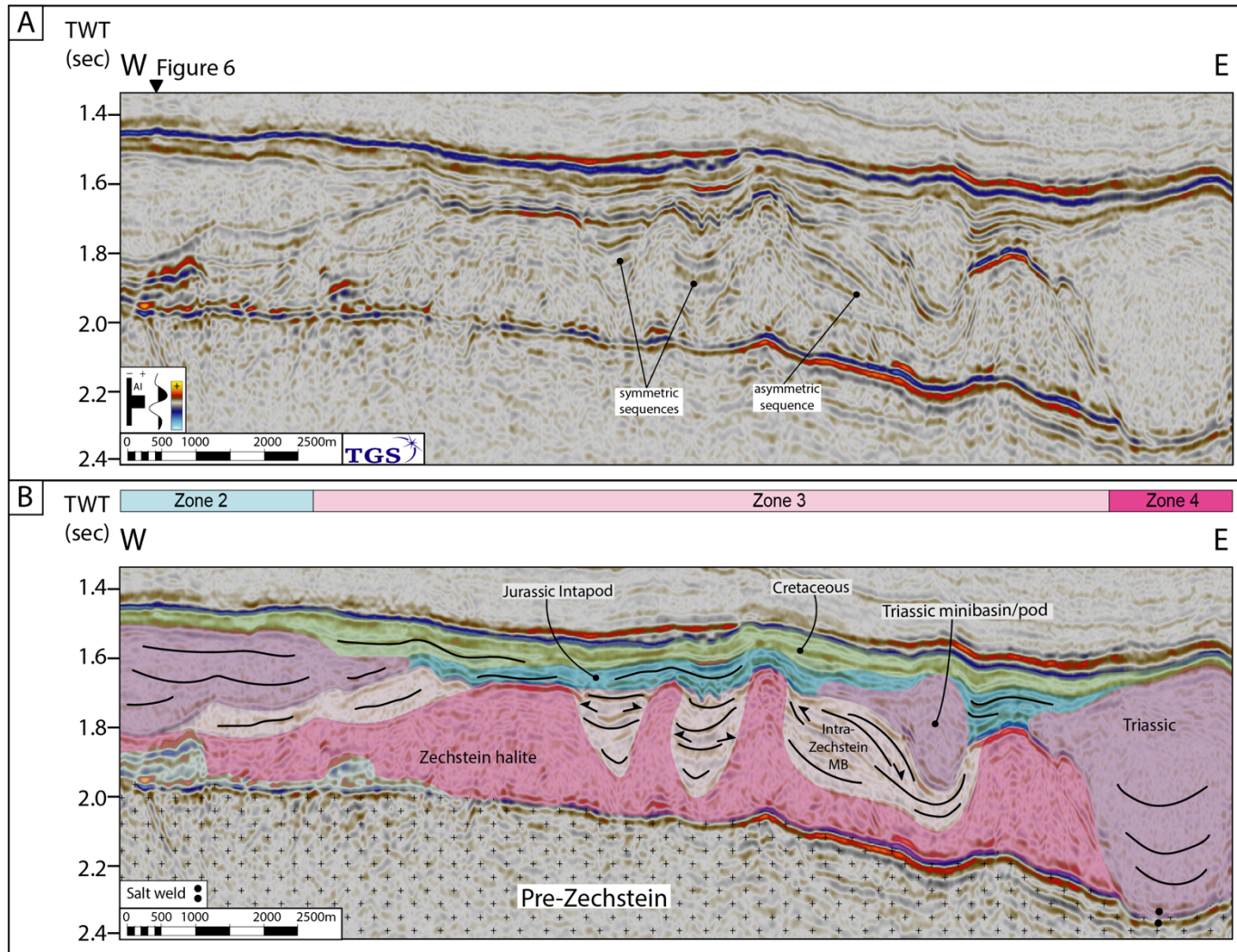
712

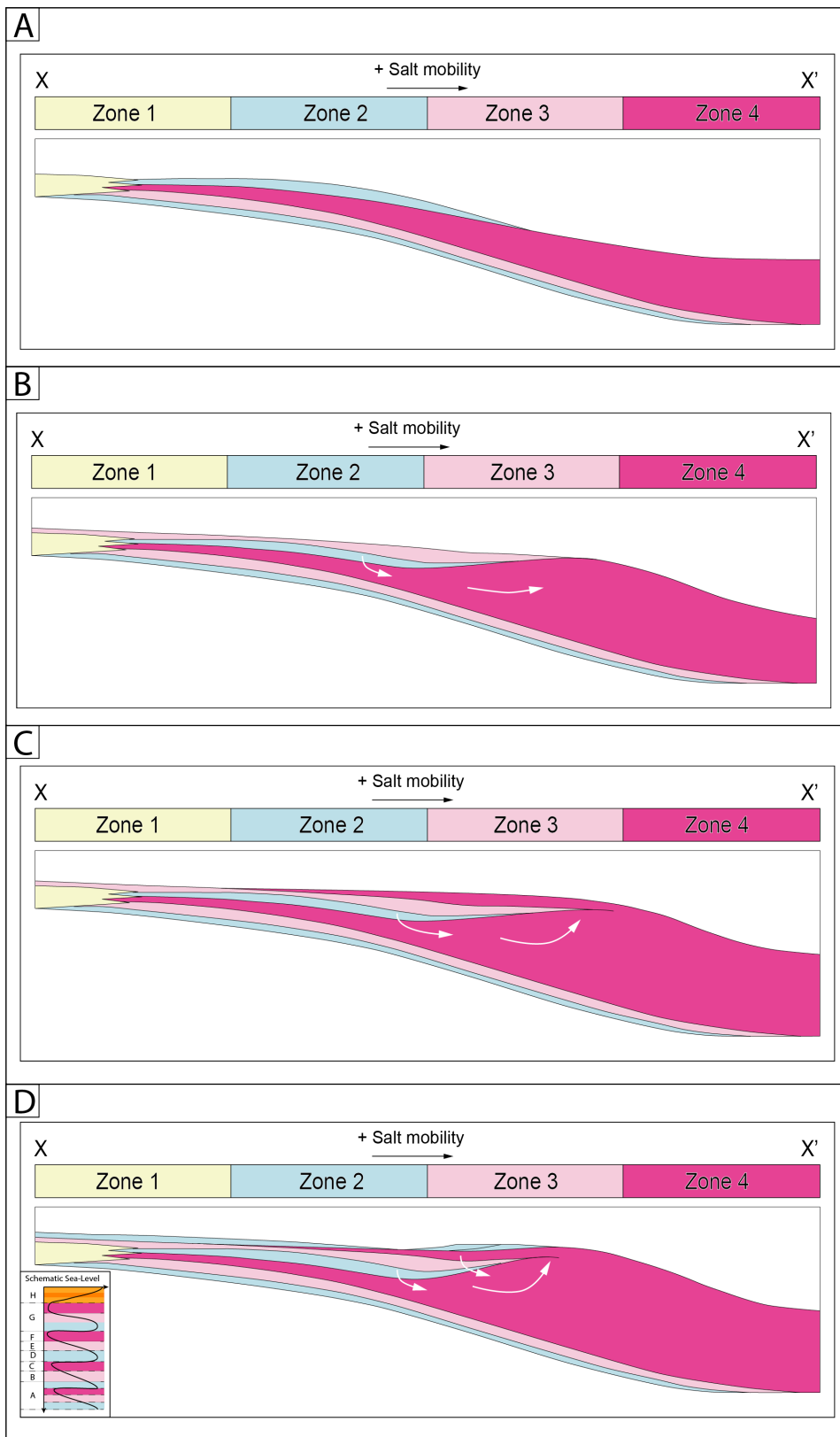
713

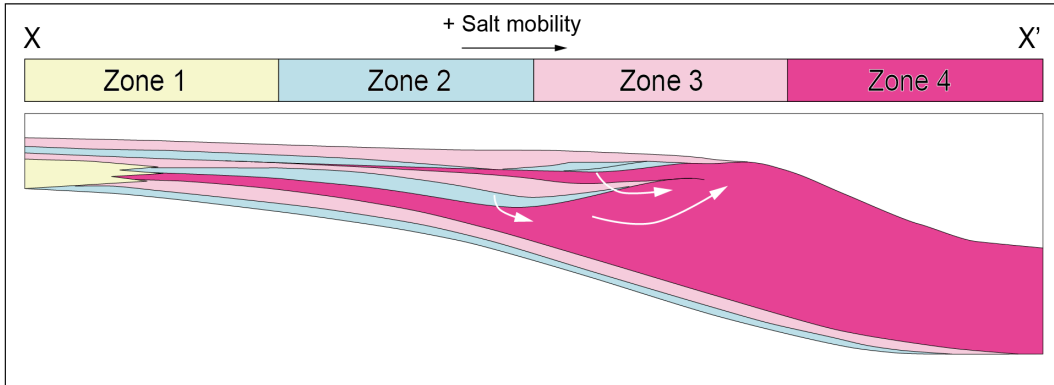
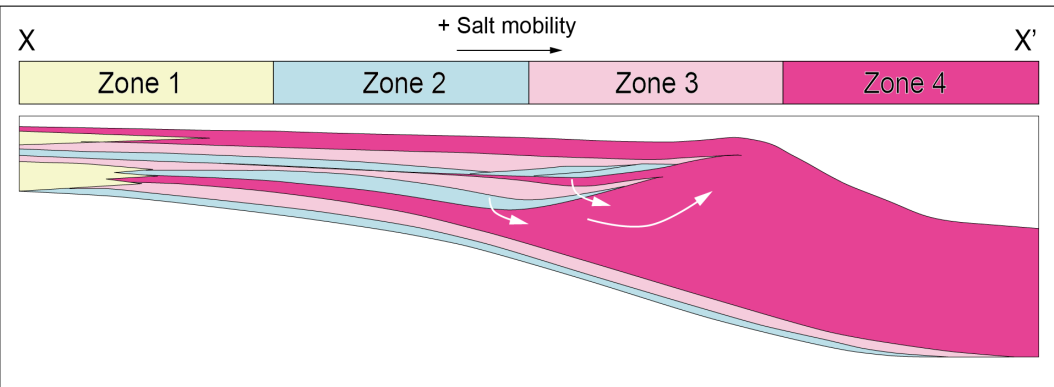
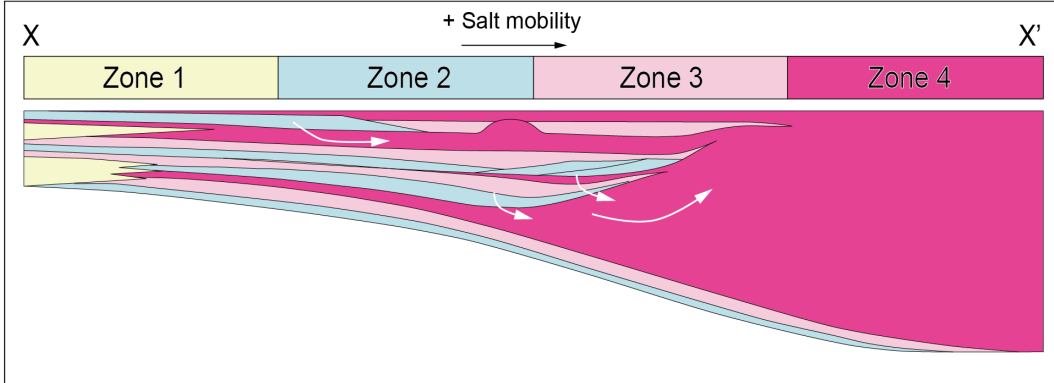


717 Figure 8







E**F****G****H**